PAPER

Check for updates

Formation of 3D Cr$_2$C through solid state reaction-mediated Al extraction within Cr$_2$AlC/Cu thin films†

Clio Azina, [ID] *[a] Justinas Palisaitis,[b] Dimitri Bogdanovski, [ID] [a] Tim Bartsch,[a] Rajib Sahu, [ID] [a,c] Christina Scheu,[c] Per O. Å. Persson, [ID] [b] Per Eklund [ID] [b,d] and Jochen M. Schneider [ID] [a]

We report on the formation of the Cr$_2$C compound using chemical etching-free methodology to extract Al from a Cr$_2$AlC MAX phase thin film. Cr$_2$AlC/Cu assemblies were deposited on sapphire substrates, using magnetron sputtering, and were subsequently annealed in vacuum. The Al from the MAX phase was shown to diffuse into Cu resulting in the formation of Al$_4$Cu$_9$ and causing the MAX phase to collapse into Cr$_2$C grains. These carbide grains were characterized by transmission electron microscopy and the interatomic distances extracted were in good agreement with *ab initio* calculations predicting the equilibrium volume of the Cr$_2$C phase.

1. Introduction

MAX phases constitute a family of ternary nanolaminated compounds given by the formula M$_{n+1}$AX$_n$ where M is a transition metal, A is a group A element, X is either carbon or nitrogen, and n = 1, 2, or 3.[1] This family of ceramics has attracted significant attention due to their exceptional properties which bridge the gap between metals and ceramics.[2,3] The unusual set of properties that MAX phases possess is a result of their hexagonal crystal structure and bonding, specifically their charge density modulation.[4] Indeed, MAX phases are characterized by strong metallic-covalent M–X bonds and weaker M–A bonds.[5] In the case of Al-containing MAX phases, such as Cr$_2$AlC or Ti$_2$AlC, the weakly bonded Al has been shown to diffuse out of the MAX phase when placed in oxidizing environments at high temperatures.[6,7] The weak nature of the M–A bonds has also led to the discovery of the MAX phases' 2D derivatives, MXenes.[8,9]

MXenes are 2D materials which are mostly obtained by chemical etching of the A-layers.[10–14] As the A-elements are etched away, the 2D M–X slabs are functionalized with terminations which are dependent on the etchant.[15] The resulting 2D materials can then be extracted and characterized further. MXenes have shown potential for a variety of applications, in particular electromagnetic shielding,[16] and energy-related ones, such as catalysis,[17] supercapacitors,[18,19] and batteries.[18,20]

While there are currently more than 100 ternary MAX phases reported,[21] not all MAX phases are found to form MXenes.[22] In fact, Cr-based MAX phases such as Cr$_2$AlC[23] and Cr$_2$GaC[24] were proven to be difficult to etch, when compared to Ti-based MAX phases such as Ti$_2$AlC,[25] Ti$_3$AlC$_2$,[26,27] and Ti$_3$SiC$_2$.[14] A number of studies, based on *ab initio* calculations, have discussed the potential of Cr$_2$C MXenes with particular focus on their electronic and magnetic properties,[28–30] their catalytic activity,[31,32] and on their use for batteries.[33] Attempts at synthesizing Cr$_2$C have been reported by Tran *et al.* starting from Cr$_2$GaC by chemical etching using hydrofluoric acid (HF),[24] and by Zou *et al.* starting from Cr$_2$AlC also using chemical etching (H$_2$SO$_4$ and LiF).[34] While etching Cr$_2$GaC was not successful, etching Cr$_2$AlC led to the formation of Cr$_2$CO$_2$, in which O replaced Al. Therefore, etching in aqueous environments is not optimal for the formation of non-oxidized Cr$_2$C MXenes.

Several studies have investigated alternative methods to produce different MXenes without the use of F-based substances (HF, LiF). Li *et al.* reported the synthesis of Ti$_3$C$_2$Cl$_2$ MXenes by prolonged reaction of Ti$_3$AlC$_2$ with ZnCl$_2$ which was further extended to different A-elements and molten salts.[14] Another option reported by Ding *et al.* involved the

[a] Materials Chemistry, RWTH Aachen University, Kopernikusstr. 10, 52074 Aachen, Germany. E-mail: azina@mch.rwth-aachen.de
[b] Thin Film Physics Division, Department of Physics, Chemistry and Biology (IFM), Linköping University, SE-581 83 Linköping, Sweden
[c] Max-Planck-Institute for Sustainable Materials, Max-Planck-Str. 1, 40237 Düsseldorf, Germany
[d] Inorganic Chemistry, Department of Chemistry - Ångström Laboratory, Uppsala University, Box 538, SE-751 21 Uppsala, Sweden
†Electronic supplementary information (ESI) available. See DOI: https://doi.org/10.1039/d4nr03664f

intercalation of species into the layered structure to increase the distance between slabs which can facilitate delamination into single layers.[12] In all these cases, the 2D MXenes were accompanied by surface terminations. Sahu *et al.* reported the formation of MBene regions during magnetron sputtering of MoAlB which is a structurally similar material to MAX phases.[35] It was shown that the MoB MBene formed close to AlO_x phases by Al deintercalation because of the Al affinity with O. This method enables direct MBene synthesis and does not involve etchants or intercalants, which leads to termination-free MBenes. Therefore, using a getter material to attract Al can allow for Al removal from MAB and/or MAX phases in order to produce MBenes and/or MXenes.

Herein, we report, for the first time, the formation of 3-dimensional Cr_2C by Al extraction from a Cr_2AlC thin film using Cu as a getter material. The formation of Cr_2C was enabled by vacuum annealing and therefore, did not involve any chemical etching step, and was confirmed by a combination of microscopy and density functional theory approaches.

2. Methods

Cr_2AlC thin films of ~400 nm in thickness were deposited by magnetron sputtering in a lab-scale high vacuum deposition chamber (base pressure $<1 \times 10^{-4}$ Pa). A powder metallurgical composite target (50 mm $\varnothing$) with a stoichiometry of 2 : 1 : 1 provided by Plansee Composite Materials GmbH, Germany, was operated in direct current magnetron sputtering (DCMS). 10×10 mm^2 $Al_2O_3(0001)$ substrates were rotated and kept at 650 °C during deposition to promote crystallization of the MAX phase. The working pressure was set to 0.55 Pa in presence of Ar and the power used on the Cr–Al–C target was set to 200 W. The thickness of ~400 nm was achieved after 20 min of deposition. After deposition the samples were left to cool overnight. Then, Cu was deposited from an elemental target (Gemmel Metalle, ≥99.95%) which was operated at 200 W in DCMS for 3 min to achieve a thickness of ~190 nm. Cu was deposited at a working pressure of 0.55 Pa, at room temperature to avoid diffusion.

In order to track changes in the assemblies with temperature, *in situ* X-ray diffraction (XRD) during heating was carried out in a Bruker AXS D8 Discover X-ray diffractometer with an integrated General Area Detector Diffraction System (GADDS). The diffractometer was equipped with an Anton Paar DHS 1100 heating stage. The measurements were carried out using Cu Kα radiation, in vacuum (<1 Pa). The incident angle was 15° and the measurements were carried out over the 2θ range of 30–50°, using 30° frames, and a collection time of 5 min per frame. The samples were heated up to 700 °C in 50 °C steps and the temperature was left to stabilize for 5 min before each measurement.

The structure of the annealed film was evaluated by XRD using a Panalytical Empyrean diffractometer with Cu Kα radiation in Bragg–Brentano geometry. Data were collected in the 10–70° 2θ range with a step size of 0.03° and a collection time of 96 s per step. An omega offset of −2° was used to remove the contribution of the substrate. Cr_2AlC/Cu samples were vacuum-annealed in a Nabertherm tube furnace. The annealing program consisted of heating the sample to 620 °C for 10 h followed by cooling to room temperature. The heating and cooling rates were set to 10 °C min^{-1} and the average pressure during annealing was $<1 \times 10^{-4}$ Pa.

For scanning transmission electron microscopy (STEM) analysis, cross-sectional lamellae were extracted from as-deposited and annealed samples using a FEI Helios NanoLab dual-beam focused ion beam (FIB) microscope. The sample microstructure and elemental distribution were investigated at the atomic level using high-angle annular dark field (HAADF) STEM imaging, energy-dispersive X-ray spectroscopy (EDX) and electron energy-loss spectroscopy (EELS) mapping. Investigations were performed using the Linköping double Cs-corrected FEI Titan^3 60-300, operated at 300 kV, equipped with a Super-X EDX system and Gatan GIF Quantum ERS post-column imaging filter. Atomically resolved HAADF-STEM imaging was acquired by using a 21.5 mrad convergence semi-angle providing sub-Ångström resolution probes with ~100 pA beam current. The HAADF-STEM angular detection was set to 46–200 mrad range. EDX spectrum images of 256 × 256 pixels were recorded in 3 min using 0.3 nA probe current in cumulative mode. Elemental Cr-Kα, Al-Kα, and Cu-Kα distribution maps were extracted from the STEM-EDX spectrum images. EELS spectra were acquired for 1 min using a 0.5 eV per channel energy dispersion, 5 s pixel dwell time, and a 55 mrad collection semi-angle. Characteristic C-K and Cr-L edges were obtained by background subtraction using a power law.[36]

The calculations were performed using a density-functional theory approach,[37,38] as implemented in the Vienna *ab initio* Simulation Package (VASP, version 5.4.4, University of Vienna),[39–41] with the resulting output post-processed by other programs, as will be described below. The projector-augmented wave (PAW) method[42,43] with a plane-wave cutoff energy of 500 eV was used for basis set construction, while electronic exchange and correlation were treated by employing the standard parametrization of the generalized gradient approximation by Perdew, Burke and Ernzerhof (PBE).[44] The valence electron configuration utilized for the individual atomic potentials was $4s^23d^43p^6$ for Cr, $3s^23p^1$ for Al and $2s^22p^2$ for C, thus incorporating the 3p "semi-core" states of Cr, as specified in the respective atomic potential files. The dimensions of the k-mesh spanning the Brillouin zone (BZ) and constructed with the Monkhorst–Pack approach[45] were specified as 13 × 13 × 2, which ensured both energetic and force convergence within 5 meV and 0.6 meV per atom, respectively, as verified by convergence tests. Integration over the BZ was performed *via* the Methfessel-Paxton method.[46]

The initial structural model for Cr_2AlC was obtained from literature,[47] with removal of the Al atoms resulting in the initial models for the MXene-like Cr_2AlC systems. All systems underwent full structural optimization, and the total energy of the optimized system was used to calculate the energy of for-

mation at the ground state *vs.* the constituent elements per eqn (1):

$$E_f(product) = \sum E_{tot}(products) - \sum E_{tot}(reactants) \quad (1)$$

with E_f as the formation energy and E_{tot} the total energies of the respective systems. For the reactants, elemental Cr (body-centered cubic structure), Al (face-centered cubic) and graphene as the C allotrope of choice were considered. In the case of graphene, the D3-BJ dispersion correction[48] was utilized to account for inter-sheet van der Waals interactions. Both the actual interatomic distances and projected in-plane distances for comparison with TEM data were extracted from the optimized systems.

It must be noted that Cr_2AlC has been reported to be antiferromagnetic in the ground state;[49] however, our calculations of the total energy show a difference between the non-spin polarized case and the energetically more favorable antiferromagnetic case of <50 meV, or approx. 6 meV per atom. Considering this small difference and the significantly higher computational cost of spin-polarized calculations particularly for lattice dynamics simulations (outlined below), which would have been prohibitive, the non-spin polarized approach was used throughout for consistency across the different simulation runs.

To obtain Gibbs' free energies of formation as a function of temperature, quasi-harmonic lattice dynamics simulations employing VASP as the main quantum-mechanical program and phonopy (version 2.11.0, University of Kyoto)[50] as a post-processor were performed. To this end, a set of supercells of roughly cubic shape with $a \approx b \approx c \approx 10$ Å was automatically generated, introducing displacements on the order of 0.02 Å from the equilibrium position of each symmetry-inequivalent atom. The exact number of displacements strongly depends on the space group of the underlying system. For each supercell, a static VASP calculation was performed to obtain the interatomic force constants, which were then processed by phonopy across all simulation runs (for each displacement) to yield a force constant matrix, from which the phonon frequencies can be obtained. From these, the lattice vibration contribution to the Helmholtz free energy, A_{ph} was calculated, which together with the ground-state energy E_{tot} given by VASP provides the dominant part of $A(V,T)$. The aforementioned set of simulation runs for distinct supercells with unique displacements was repeated for a set of different volumes besides the equilibrium volume, accounting for the volume dependence of $A(V,T)$. Fitting this data to the Birch–Murnaghan equation of state[51,52] then yields the temperature dependence as well, so that the Gibbs free energy for a given system was obtained. The Gibbs free energies of formation for a given reaction, $\Delta G(T)$ were then calculated as per eqn (1), with G replacing E_{tot}. We refer to prior literature for further methodological details on this approach.[53,54]

Finally, bonding analysis based on the Crystal Orbital Hamilton Population (COHP) technique[55] using the LOBSTER package (version 4.0.0., Institute of Inorganic Chemistry, RWTH Aachen University)[56–58] was performed to quantify the interatomic interactions in the examined systems. To this end, static VASP simulations of the optimized systems provided the PAW-based wavefunctions of the individual systems, which were then projected onto local atomic basis sets, allowing for the treatment of localized interatomic interactions (*i.e.*, chemical bonds). This results in integrated crystal orbital Hamilton population (ICOHP) values, describing the strength of an interaction up to the Fermi level, with more negative values signifying stronger bonds. While not equal to the "true" bond strength, which is hard to quantify, the ICOHP value is strongly correlated with the latter and is routinely used as a descriptor for it.[59–61]

3. Results and discussion

The XRD patterns of the as-deposited Cr_2AlC (400 nm)/Cu (190 nm) thin film assembly as well as the patterns collected during *in situ* heating are shown in Fig. 1 (extended step size in Fig. S1†). As the temperature was progressively increased, the structural changes occurring in the sample could be identified. The as-deposited sample exhibited characteristic peaks of the MAX phase (given by the blue dashed lines) at 36–37° and ~42° corresponding to the (100)/(101) and (103)/(006) reflections, respectively. Additionally, the (111) Cu reflection was identified at ~43°. As the temperature increased the signals of the MAX phase and Cu began to decrease in intensity and shift to lower 2θ angles, either because of the formation of solid solutions or because of the thermal expansion of the lattice upon heating. At 200 °C, the Cu reflection disappeared, suggesting that the Cu had been consumed. At 300 °C, a peak
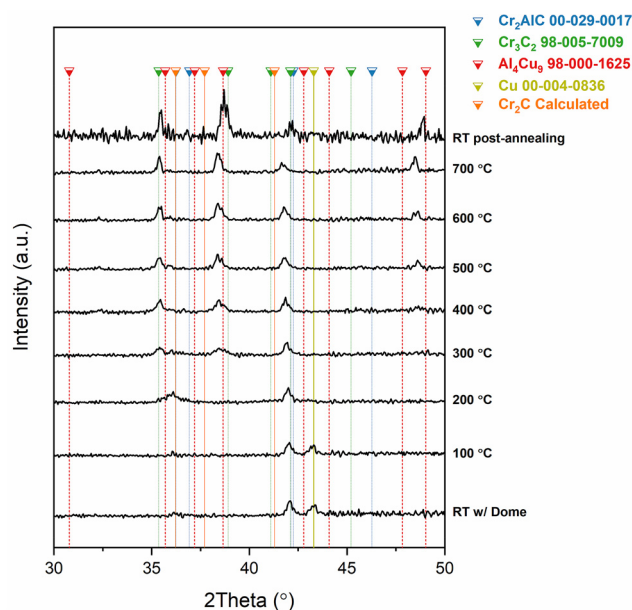

Fig. 1 XRD patterns obtained during, and after, *in situ* XRD annealing of as-deposited Cr_2AlC/Cu assemblies, up to 700 °C with 100 °C steps.
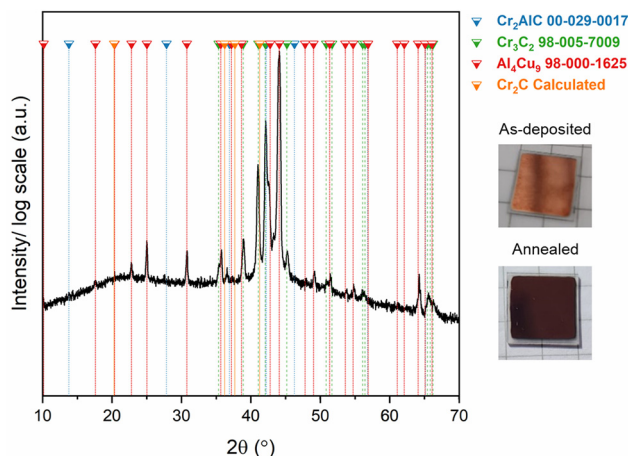
Fig. 2 XRD pattern of the Cr_2AlC/Cu assembly post-annealing at 620 °C for 10 h, in vacuum. Photographs of the Cr_2AlC/Cu assembly surface before and after annealing.

and a broad band appeared at approx. 35° and 38°, respectively, suggesting crystallization of a new phase, which could be indexed as Cr_3C_2. Their intensity increased with increasing temperature, while their full width at half maximum decreased. Based on identification carried out on the sample post-annealing, the peak was indexed as (310) of Al_4Cu_9. Another peak which could be indexed as (332) of Al_4Cu_9 appeared between 350–450 °C. The MAX phase peaks at ~42° were shifted to lower 2θ angles during heating and returned to their original peak position post-annealing, confirming that the shift was due to thermal expansion.

To enhance the diffusion of species, the Cr_2AlC/Cu assemblies were annealed in a vacuum furnace for 10 h at 620 °C. The appearance of the assemblies before and after vacuum annealing are shown in Fig. 2. As can be seen, the appearance changed drastically from metallic copper to a darker color. The XRD pattern of the annealed sample is also shown in Fig. 2. The MAX phase and Al_4Cu_9 phases were indexed, in addition
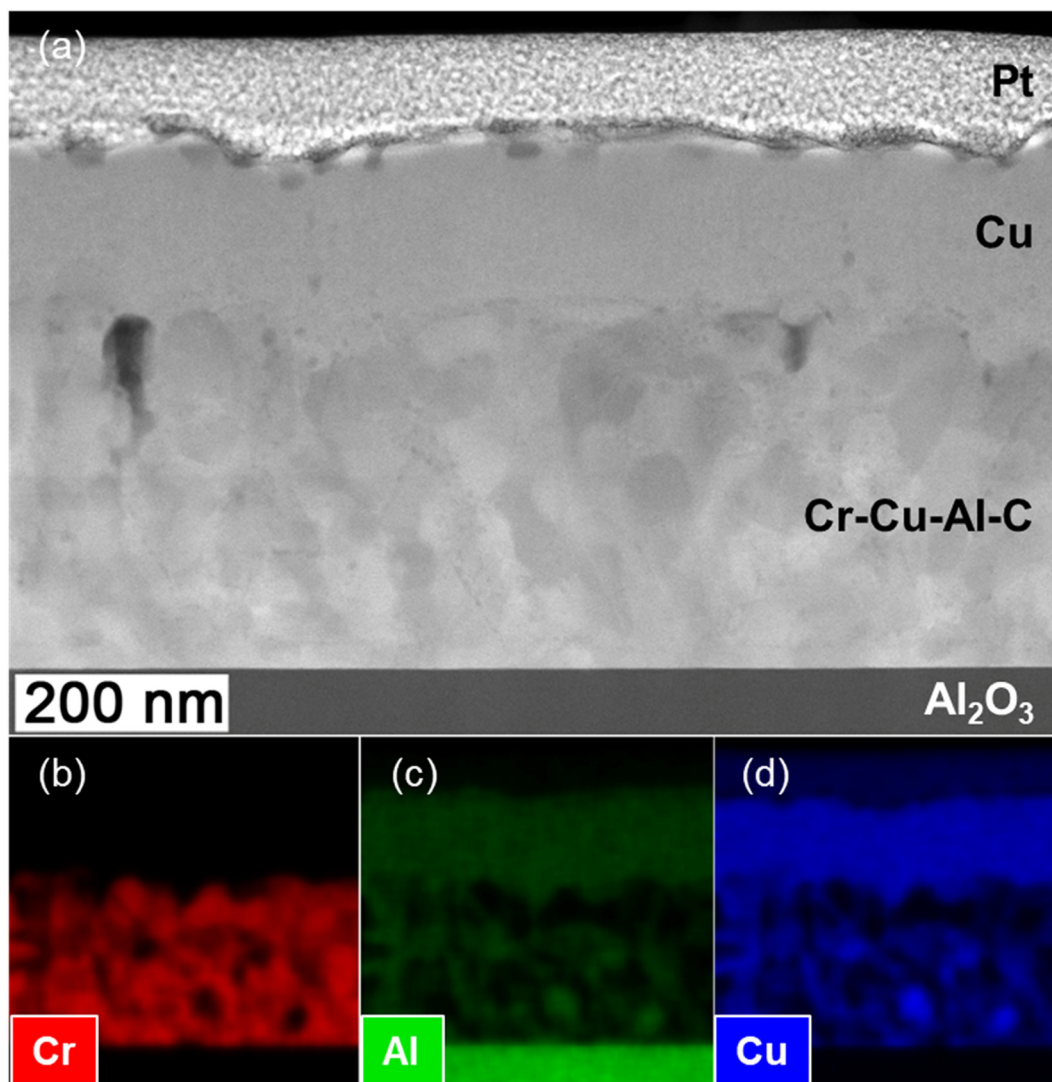

Fig. 3 (a) HAADF-STEM micrograph of the annealed Cr_2AlC/Cu assembly, and (b)−(d) corresponding EDX maps.

to Cr_3C_2, which is in good agreement with observations made during the *in situ* XRD, in Fig. 1.

It is well known from oxidation experiments that Al is mobile and tends to diffuse out of Cr_2AlC when subjected to high-temperature oxidizing environments.[6,7,62] In fact, one of the major challenges when oxidizing Cr_2AlC at high temperatures is the decomposition of the MAX phase into Cr-carbides as Al leaves the MAX phase.[6,7,63,64] Similarly, as Al interacts with Cu to either form a solid solution or the intermetallic phase (Al_4Cu_9), the MAX phase is expected to be Al-depleted and therefore decompose into Cr-carbides. Evidence for the formation of Cr_2C based on X-ray diffraction data (Fig. 2 and S2†) could not be obtained.

Fig. 3 shows a STEM image and corresponding EDX maps obtained from a lamella extracted from the vacuum annealed sample. STEM images and corresponding EDX maps of the as-deposited Cr_2AlC can be seen in Fig. S3.† The as-deposited films exhibited a homogeneous distribution of Cr and Al throughout the thickness of the film, as well as a clear interface between the MAX phase film and the top Cu layer, indicating that no intermixing occurred during deposition. From the STEM image of the annealed sample in Fig. 3(a) one can notice that the Cu layer deposited on top of the MAX film is still present, therefore, confirming that the MAX phase has access to a continuous supply of Cu.[65] It is evident from the maps in Fig. 3(b)–(d) that a phase separation occurred since Cr-rich particles are separated from Cu–Al-rich particles, as there is no indication for the formation of Cu–Al alloys within MAX phase grains. In fact, the Cu–Al alloys are found in the vicinity of Cr-rich grains (Cr_2C, Cr_3C_2 or Cr_2AlC) as evidenced
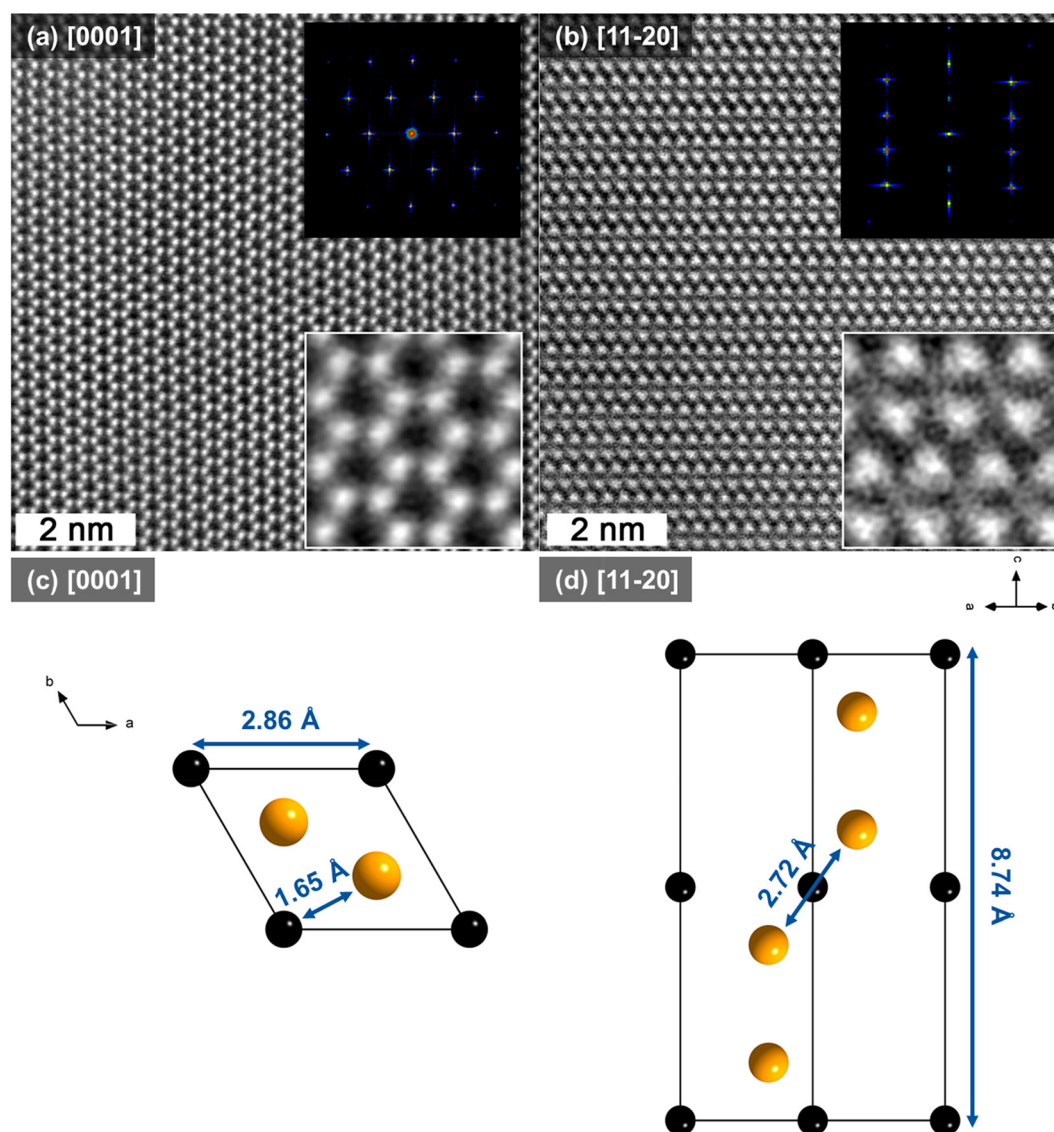

Fig. 4 HAADF–STEM images along (a) [0001] and (b) [11−20] zone axes and corresponding FFT patterns. (c) and (d) correspond to the representation of the cell along [0001] and [11−20]. Black spheres represent C and orange spheres represent Cr atoms.

on the EDX maps in Fig. 3. It can also be seen that Cr-rich grains exhibit little to no Al presence, consistent with the formation of Cr_2C or Cr_3C_2. The formation of Cr_2C is supported by the EELS spectrum, shown in Fig. S3,† where Cr-rich areas/grains contain Cr and C in a 2:1 ratio which corresponds to the stoichiometry of a Cr_2C carbide. However, based on the XRD patterns in Fig. 1 and 2, no clear indication of the presence of the Cr_2C phase could be deduced while Cr_3C_2 was indexed in both the *in situ* and *ex situ* measurements.

To confirm the phase that has formed after Al removal from Cr_2AlC, atomically resolved STEM images were acquired from Cr-rich grains (Fig. S4†) where little to no Al is present, and are presented in Fig. 4. Two perpendicular zone axes are shown and the corresponding calculated fast Fourier transform (FFT) patterns are provided as insets. In Fig. 4(a) one can observe the typical honeycomb structure characteristic of a hexagonal structure, with $n = 1$. The lack of chemical contrast in addition to the EELS spectrum (Fig. S3†) suggests that the bright regions correspond to Cr and that the structure corresponds to Cr_2C. Indeed, the Cr to C ratio of 2:1 could suggest the formation of carbon-deficient Cr_3C_2, however, the STEM images and corresponding FFTs do not correspond to the Cr_3C_2 structure but rather the Cr_2C one. Along the [11−20] zone axis, one can observe the Cr_2C slabs which remain intact after Al

removal from the starting MAX phase. The spacing between Cr_2C slabs is smaller by nearly half than in the MAX phase due to Al removal. This suggests, that part of the MAX phase structure has collapsed into Cr_2C. To compare the measured projected bond distances with predictions, a Cr_2C cell was simulated by DFT by removing Al from a Cr_2AlC cell and allowing the configuration to relax. The resulting structure is depicted in Fig. 4 along (c) [0001] and (d) [11−20].

The interatomic distances were extracted from the simulated cell (Fig. 4(c) and (d)) and compared with those extracted from the corresponding FFTs from the STEM data in Fig. 4. The resulting projected distances are provided in Table 1. One can notice that the experimentally deduced values are in good agreement with the ones predicted by theory. In fact, the deviations for projected bond distances deduced from calculations and TEM is 0.6% for Cr–Cr. Interestingly, the largest difference is measured for intra-slab Cr–Cr bonds where the experimentally deduced distance is ~2.2% smaller than the theoretical one. According to Paier *et al.*, this deviation has to be expected considering the exchange correlation functionals employed here.[66]

A complete bonding analysis was carried out to assess whether large differences would be observed between Cr_2C slabs in the case of a free standing MXene and in the case of the MAX phase. Fig. 5 gathers the actual (*i.e.* unprojected) interatomic distances, the average ICOHP per bond and the sum of all ICOHP values in the unit cell up to and including the second coordination shell, thus totaling all bonds, for Cr_2AlC and Cr_2C. First of all, one may notice that the interatomic distances (Fig. 5(a)) in both Cr_2AlC and Cr_2C are only slightly different, which is to be expected considering the electronic structure has been rearranged because of Al removal. Then, the average ICOHP values per bond, in Fig. 5(b) show that Cr–Cr and Cr–C bonds in the Cr_2C slabs have weakened compared to those in Cr_2AlC, while the C–C bonds were

Table 1 Projected distances determined by TEM and DFT

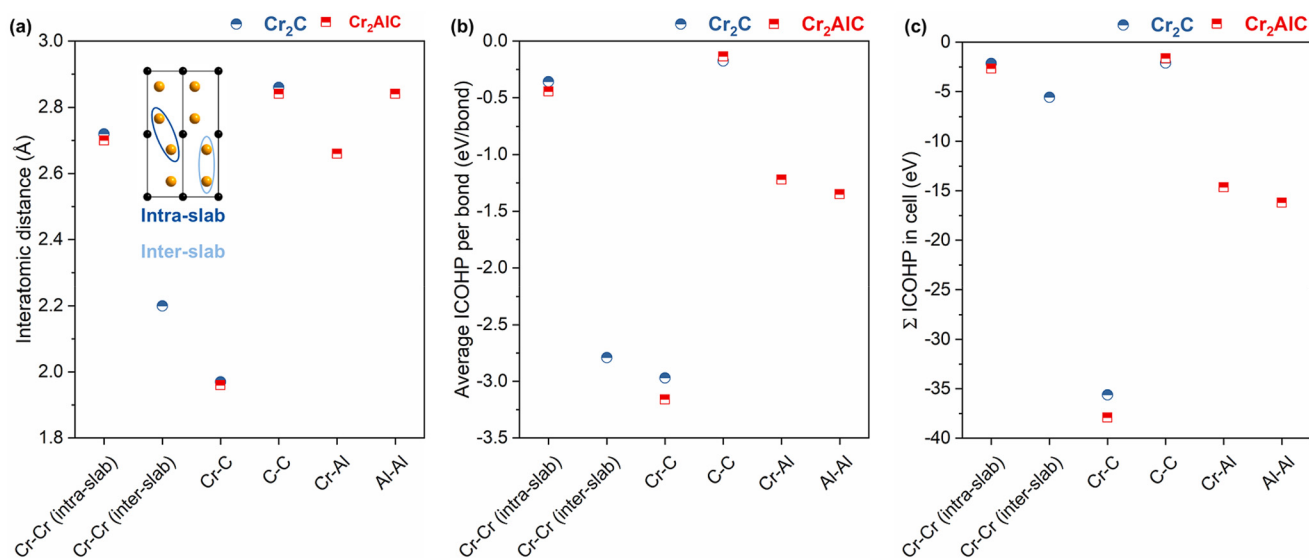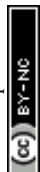| Distances	Cr_2C (STEM) (Å)	Cr_2C (DFT) (Å)	Relative deviation (%)
Cr–Cr(0001)	1.66 ± 0.05	1.65	0.6
Cr–Cr(11−20)	2.66 ± 0.05	2.72	2.2
a parameter	2.7 ± 0.1	2.86	5.6
c parameter	9.5 ± 0.1	8.74	8.7

Fig. 5 (a) Interatomic distances, (b) average ICOHP per bond, and (c) sum of ICOHP in the 1st and 2nd coordination spheres of the cell for Cr_2AlC and Cr_2C.

slightly strengthened. Strong Cr–Cr inter-slab bonds (see inset in Fig. 5 for visualization) are also observed compared to Cr–Al bonds in the MAX phase which is because the Cr–Cr bonds are shorter. The sum over all interactions are shown in Fig. 5(c) and show a similar trend as for the individual interactions, despite a weaker interaction for the Cr–Cr inter-slabs in Cr_2C compared to the Cr–Al and Al–Al interactions in the MAX phase.

As stated above, the oxidation resistance of Cr_2AlC has been widely investigated and it is common knowledge that upon Al depletion, Cr_2AlC decomposes into stable Cr-carbides, namely Cr_7C_3 and Cr_3C_2.[6] While the mechanism of Al extraction is similar to that which occurs during oxidation, the local formation of Cr_2C is observed here. The temperature-dependent Gibbs free energies of formation of different Cr-carbides upon Al removal from Cr_2AlC are provided in Fig. 6. One can see

Fig. 6 Gibbs' free energy of formation curves of decomposition routes of Cr_2AlC derived from lattice dynamics simulations.

that the most stable carbide formed is expected to be Cr_3C_2, which is in good agreement with the XRD (Fig. 1, S1, and 2†). Cr_2C formation, however, is not favorable averaging at ~100 kJ per mol at 900 K (~1 eV per atom), which suggests that the compound is metastable. While the transformation of Cr_2C into a more stable carbide such as Cr_3C_2 was not investigated here, based on the Gibb's free energies presented herein, it is likely that this transformation occurs.

The main difference between the process presented herein and oxidation are the temperature at which the samples are annealed (620 vs. ≥1000 °C), the environment (air vs. vacuum), and the duration of the process (10 h vs. 1–2 h). Considering that oxidation occurs at temperatures ≥1000 °C, the Al diffusion is much more rapid than at 620 °C. The rapid depletion in Al is expected to destabilize the MAX phase structure abruptly causing it to transform into a stable carbide (e.g. Cr_3C_2 and/or Cr_7C_3, as both have been reported experimentally[6,7]). Depleting the Al progressively, however, was shown here to result in the formation of Cr_2C by collapse of the MAX phase. Another important difference between the two cases is the getter element, Cu for this work and O during oxidation. The resulting compound will either be a ductile and expandable Cu alloy or solid solution for the former, while a brittle Al_2O_3 will be the resulting compound for the latter. These compounds can also affect the final product after Al-extraction.

The metastable Cr_2C phase coexists with Cr_2AlC, Cr_3C_2, Al_4Cu_9, and a Cu–Al solid solution. As observed on the HAADF-STEM micrographs, upon Al removal, part of the MAX phase had collapsed as the Cr–Cr distance between slabs was much smaller compared to when Al was still present. Furthermore, we observed that Cr-rich grains are directly adjacent to a Cu-containing phase. By combining HAADF-STEM observations and calculations we are suggesting the following mechanism for the formation of the metastable Cr_2C phase, see Fig. 7. Al diffuses out of the MAX phase into the Cu layer to
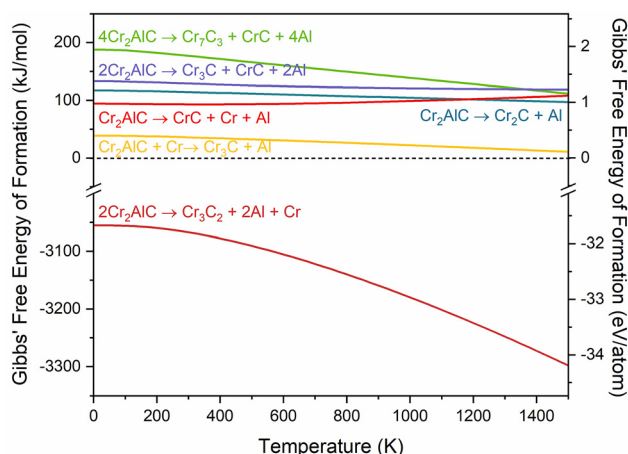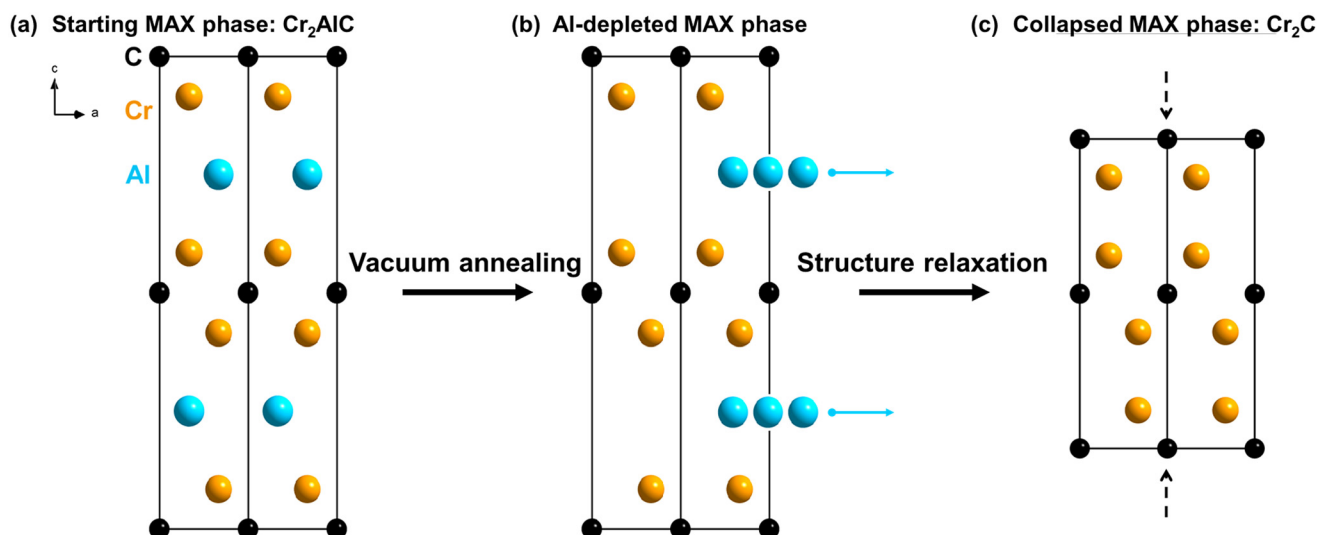

Fig. 7 Schematic of (a) starting Cr_2AlC MAX phase, (b) Al-depleted Cr_2AlC, and (c) collapsed MAX phase structure resulting in Cr_2C.

either form a solid solution or the intermetallic Al_4Cu_9 phase. As Al is extracted from the MAX phase, the Cr_2C slabs collapse as is evidenced by the smaller Cr–Cr inter-slab distances.

4. Conclusion

We reported the formation of metastable Cr_2C obtained by Al extraction within a Cr_2AlC/Cu thin film, without the use of chemical etching. While oxidation studies have reported the decomposition of the MAX phase into Cr_7C_3 and Cr_3C_2 upon Al depletion, the observations made herein show that the metastable Cr_2C can also form upon Al removal. Indeed, vacuum annealing of Cr_2AlC/Cu assemblies resulted in a multiphase film composed of Cr_2C, Cr_2AlC, Cr_3C_2, Al_4Cu_9 and a solid solution of Al in Cu. HAADF-HRSTEM allowed determining the interatomic distances in the newly formed Cr_2C which were in good agreement with distances extracted from *ab initio* calculations. The bonding analysis suggests that the interactions between Cr–Cr intra-slabs in Cr_2C and Cr–Cr in Cr_2AlC are similar as the sum of the ICOHP values varies between −2.1 and −2.6 eV. However, the distance between slabs has significantly shrunk (2.2 Å in Cr_2C instead of 2.6 Å for the Cr–Al distance in the MAX phase) because of the Al removal which has caused the MAX phase to collapse into Cr_2C. While the final product is a multiphase film, optimization of the process conditions (use of powder instead of thin films, annealing temperature and duration, Cu volume fraction, *etc.*), may result in a higher fraction of Cr_2C enabled by efficient Al extraction.

Author contributions

C. A.: conceptualization, data curation, formal analysis, investigation, methodology, funding acquisition, project, administration, visualization, writing original draft. J. P.: formal analysis, data curation, investigation, methodology, writing – review & editing. D. B.: formal analysis, investigation, methodology, writing – review & editing. T. B.: formal analysis, investigation, writing – review & editing. R. S.: formal analysis, writing – review & editing. C. S.: supervision, writing – review & editing. P. O. Å. P.: resources, supervision, funding acquisition, writing – review & editing. P. E.: resources, funding acquisition, writing – review & editing. J. M. S.: resources, supervision, writing – review & editing.

Data availability

The data supporting this study are available within the article and the ESI.†

Conflicts of interest

There are no conflicts of interest to declare.

Acknowledgements

References

1 M. W. Barsoum, *Prog. Solid State Chem.*, 2000, **28**, 201.
2 M. Radovic and M. W. Barsoum, *Am. Ceram. Soc. Bull.*, 2013, **92**, 20.
3 J. Gonzalez-Julian, *J. Am. Ceram. Soc.*, 2021, **104**, 659.
4 M. Sokol, V. Natu, S. Kota and M. W. Barsoum, *Trends Chem.*, 2019, **1**, 210.
5 M. Magnuson and M. Mattesini, *Thin Solid Films*, 2017, **621**, 108.
6 D. E. Hajas, M. To Baben, B. Hallstedt, R. Iskandar, J. Mayer and J. M. Schneider, *Surf. Coat. Technol.*, 2011, **206**, 591.
7 C. Azina, M. Poll, D. M. Holzapfel, E. Tailleur, A. Zuber, S. Dubois, P. Eklund and J. Gonzalez-Julian, *J. Eur. Ceram. Soc.*, 2024, **44**, 4895–4904.
8 M. Naguib, M. Kurtoglu, V. Presser, J. Lu, J. Niu, M. Heon, L. Hultman, Y. Gogotsi and M. W. Barsoum, *Adv. Mater.*, 2011, **23**, 4248.
9 M. Naguib, V. N. Mochalin, M. W. Barsoum and Y. Gogotsi, *Adv. Mater.*, 2014, **26**, 992.
10 M. Naguib, M. W. Barsoum and Y. Gogotsi, *Adv. Mater.*, 2021, **33**, 2103393.
11 Y. Wei, P. Zhang, R. A. Soomro, Q. Zhu and B. Xu, *Adv. Mater.*, 2021, **33**, 2103148.
12 H. Ding, Y. Li, M. Li, K. Chen, K. Liang, G. Chen, J. Lu, J. Palisaitis, P. O. Å. Persson, P. Eklund, L. Hultman, S. Du, Z. Chai, Y. Gogotsi and Q. Huang, *Science*, 2023, **379**, 1130.
13 M. Li, J. Lu, K. Luo, Y. Li, K. Chang, K. Chen, J. Zhou, J. Rosen, L. Hultman, P. Eklund, P. O. Å. Persson, S. Du, Z. Chai, Z. Huang and Q. Huang, *J. Am. Chem. Soc.*, 2019, **141**, 4730.
14 Y. Li, H. Shao, Z. Lin, J. Lu, L. Liu, B. Duployer, P. O. Å. Persson, P. Eklund, L. Hultman, M. Li, K. Chen, X.-H. Zha, S. Du, P. Rozier, Z. Chai, E. Raymundo-Piñero,

P.-L. Taberna, P. Simon and Q. Huang, *Nat. Mater.*, 2020, **19**, 894.

15 V. Natu and M. W. Barsoum, *J. Phys. Chem. C*, 2023, **127**, 20197–20206.

16 F. Shahzad, M. Alhabeb, C. B. Hatter, B. Anasori, S. M. Hong, C. M. Koo and Y. Gogotsi, *Science*, 2016, **353**, 1137–1140.

17 I. M. Chirica, A. G. Mirea, Ş. Neaţu, M. Florea, M. W. Barsoum and F. Neaţu, *J. Mater. Chem. A*, 2021, **9**, 19589.

18 Y. Sun, D. Chen and Z. Liang, *Mater. Today Energy*, 2017, **5**, 22.

19 Q. Zhu, J. Li, P. Simon and B. Xu, *Energy Storage Mater.*, 2021, **35**, 630.

20 Z. Chen, Z. Chang, Z. Liu and N. Zhou, *Appl. Surf. Sci.*, 2022, **602**, 154375.

21 M. Dahlqvist, M. W. Barsoum and J. Rosen, *Mater. Today*, 2024, **72**, 1.

22 Y. Gogotsi and B. Anasori, *ACS Nano*, 2019, **13**, 8491.

23 O. Akinola, I. Chakraborty, H. Celio, D. Akinwande and J. A. C. Incorvia, *J. Mater. Res.*, 2021, **36**, 1980.

24 M. H. Tran, A. M. Malik, M. Dürrschnabel, A. Regoutz, P. Thakur, T.-L. Lee, D. Perera, L. Molina-Luna, K. Albe, J. Rohrer and C. S. Birkel, *Dalton Trans.*, 2020, **49**, 12215.

25 L. Liu, H. Zschiesche, M. Antonietti, M. Gibilaro, P. Chamelot, L. Massot, P. Rozier, P.-L. Taberna and P. Simon, *Adv. Energy Mater.*, 2023, **13**, 2203805.

26 L. Liu, M. Orbay, S. Luo, S. Duluard, H. Shao, J. Harmel, P. Rozier, P.-L. Taberna and P. Simon, *ACS Nano*, 2022, **16**, 111.

27 N. Goossens, K. Lambrinou, B. Tunca, V. Kotasthane, M. C. Rodríguez González, A. Bazylevska, P. O. Å. Persson, S. De Feyter, M. Radovic, F. Molina-Lopez and J. Vleugels, *Small Methods*, 2024, **8**, 2300776.

28 B. Akgenc, B. Akgenc, E. Vatansever and F. Ersan, *Phys. Rev. Mater.*, 2021, **5**, 083403.

29 C. Si, J. Zhou and Z. Sun, *ACS Appl. Mater. Interfaces*, 2015, **7**, 17510.

30 Q. Sun, Z. Fu and Z. Yang, *J. Magn. Magn. Mater.*, 2020, **514**, 167141.

31 Y. Cheng, J. Dai, Y. Zhang, Y. Zhang, Y. Song and Y. Song, *J. Mater. Chem.*, 2018, **6**, 20956.

32 I. A. M. Ibrahim, S. Abdel-Azeim, A. M. El-Nahas, O. Kühn, C.-Y. Chung, A. El-Zatahry and M. F. Shibl, *J. Phys. Chem. C*, 2022, **126**, 14886.

33 Y. Li, L. Bai, N. Ma and L. Niu, *Comput. Theor. Chem.*, 2022, **1217**, 113892.

34 X. Zou, H. Liu, H. Xu, X. Wu, X. Han, J. Kang and K. M. Reddy, *Mater. Today Energy*, 2021, **20**, 100668.

35 R. Sahu, D. Bogdanovski, J.-O. Achenbach, S. Zhang, M. Hans, D. Primetzhofer, J. M. Schneider and C. Scheu, *Nanoscale*, 2021, **13**, 18077.

36 R. F. Egerton, *Electron Energy-Loss Spectroscopy in the Electron Microscope*, 2011.

37 P. Hohenberg and W. Kohn, *Phys. Rev.*, 1964, **136**, B864.

38 W. Kohn and L. J. Sham, *Phys. Rev.*, 1965, **140**, A1133.

39 G. Kresse and J. Furthmüller, *Phys. Rev. B:Condens. Matter Mater. Phys.*, 1996, **54**, 11169.

40 G. Kresse and J. Furthmüller, *Comput. Mater. Sci.*, 1996, **6**, 15.

41 G. Kresse and J. Hafner, *Phys. Rev. B:Condens. Matter Mater. Phys.*, 1993, **47**, 558.

42 P. E. Blöchl, *Phys. Rev. B:Condens. Matter Mater. Phys.*, 1994, **50**, 17953.

43 G. Kresse and D. Joubert, *Phys. Rev. B:Condens. Matter Mater. Phys.*, 1999, **59**, 1758.

44 J. P. Perdew, K. Burke and M. Ernzerhof, *Phys. Rev. Lett.*, 1996, **77**, 3865.

45 H. J. Monkhorst and J. D. Pack, *Phys. Rev. B*, 1976, **13**, 5188.

46 M. Methfessel and A. T. Paxton, *Phys. Rev. B:Condens. Matter Mater. Phys.*, 1989, **40**, 3616.

47 J. C. Schuster, H. Nowotny and C. Vaccaro, *J. Solid State Chem.*, 1980, **32**, 213.

48 S. Grimme, J. Antony, S. Ehrlich and H. Krieg, *J. Chem. Phys.*, 2010, **132**, 154104.

49 M. Dahlqvist, B. Alling and J. Rosén, *J. Appl. Phys.*, 2013, **113**, 216103.

50 A. Togo and I. Tanaka, *Scr. Mater.*, 2015, **108**, 1.

51 F. Birch, *Phys. Rev.*, 1947, **71**, 809.

52 F. D. Murnaghan, *Proc. Natl. Acad. Sci. U. S. A.*, 1944, **30**, 244.

53 R. P. Stoffel, C. Wessel, M.-W. Lumey and R. Dronskowski, *Angew. Chem., Int. Ed.*, 2010, **49**, 5242.

54 D. Bogdanovski, P. J. Pöllmann and J. M. Schneider, *Nanoscale*, 2022, **14**, 12866.

55 R. Dronskowski and P. E. Bloechl, *J. Phys. Chem.*, 1993, **97**, 8617.

56 S. Maintz, V. L. Deringer, A. L. Tchougréeff and R. Dronskowski, *J. Comput. Chem.*, 2013, **34**, 2557.

57 S. Maintz, V. L. Deringer, A. L. Tchougréeff and R. Dronskowski, *J. Comput. Chem.*, 2016, **37**, 1030.

58 R. Nelson, C. Ertural, J. George, V. L. Deringer, G. Hautier and R. Dronskowski, *J. Comput. Chem.*, 2020, **41**, 1931.

59 G. A. Landrum and R. Dronskowski, *Angew. Chem., Int. Ed.*, 2000, **39**, 1560.

60 A. Saksena, D. Bogdanovski, H. Sahasrabuddhe, D. Music and J. M. Schneider, *Materials*, 2020, **13**, 2298.

61 S. Amano, D. Bogdanovski, H. Yamane, M. Terauchi and R. Dronskowski, *Angew. Chem., Int. Ed.*, 2016, **55**, 1652.

62 X. Chen, B. Stelzer, M. Hans, R. Iskandar, J. Mayer and J. M. Schneider, *Mater. Res. Lett.*, 2021, **9**, 127.

63 J. Gonzalez-Julian, T. Go, D. E. Mack and R. Vaßen, *J. Am. Ceram. Soc.*, 2018, **101**, 1841.

64 A. Zuber, V. Gauthier-Brunet, J. Roger, J. Gonzalez-Julian, T. Ouisse and S. Dubois, *J. Eur. Ceram. Soc.*, 2022, **42**, 2089.

65 H. Fashandi, M. Dahlqvist, J. Lu, J. Palisaitis, S. I. Simak, I. A. Abrikosov, J. Rosen, L. Hultman, M. Andersson, A. Lloyd Spetz and P. Eklund, *Nat. Mater.*, 2017, **16**, 814.

66 J. Paier, M. Marsman, K. Hummer, G. Kresse, I. C. Gerber and J. G. Ángyán, *J. Chem. Phys.*, 2006, **124**, 154709.